8th International Conference
on
Wind Turbine Noise
Lisbon – 12th to 14th June 2019

Aeroacoustic Assessment of Wind Turbine Blade Tips

M. Herr, C.-H. Rohardt and B. Faßmann
German Aerospace Center (DLR), Braunschweig, Germany, D-38108

J. M. Pereira-Gomes
DNW-NWB, Braunschweig, Germany, D-38108

Summary

The trend to large wind turbines with increased blade diameters requires efficient noise reduction to increase public acceptance and to avoid further limitations in land use or shut-down times during night. Within the German national wind energy project BELARWEA improved methods to support the design of both, aerodynamically efficient and low-noise, wind turbine rotors are developed and validated. Aeroacoustically driven 2D profile design, 3D winglet design and 2D/3D CFD and CAA analysis are supplemented by the transfer of passive noise reduction technologies from aerospace applications to wind turbine blades. Experimental demonstration and tool validation is provided in systematic evaluation steps, (i) at 2D blade sections in the Acoustic Wind-Tunnel Braunschweig (AWB) of DLR, and (ii) at 3D blade tips in the larger acoustic facility DNW-NWB, operated by the German-Dutch Wind Tunnels foundation. The current paper provides a general overview of the DNW-NWB experiments and available validation data. Beyond this, the focus is set on the aeroacoustic evaluation of a new profile contour RoH-W-18%c37 (vs. NACA 64-618 reference profile) in the 2D as well as 3D test environments. The DNW-NWB tests were conducted on two 1:6 blade tip models in both the closed (3.25 m x 2.80 m) and ¾-open wind-tunnel test sections. Numerical results from a largely non-empirical hybrid CFD/CAA airfoil noise prediction approach, as applied during the profile design process, show excellent agreement with the finally measured 2–4 dB reduction of maximum sound pressure levels.

1. Introduction

According to current knowledge, trailing-edge noise (TEN), as generated in the outer 20–25% of the rotor radius, represents the most relevant noise contributor at modern large wind turbines. Important indicators to support this statement are i) measurements of noise radiation directivities corresponding to the typical TEN cardioid-type characteristics, ii) noise source localization results at wind turbine rotor blades acquired with phased microphone arrays, and finally, iii) the experimentally proven efficiency of trailing-edge modifications on overall wind turbine noise in field measurements [19–21]. TEN at rotor blades is generally modeled as 2D problem while separating the rotor in distinct blade elements. Its key mechanism is the fluctuating pressure induced by the boundary-layer turbulent eddies and its propagation to the farfield due to the scattering from the trailing edge (TE) [10, 16]. The overall blade noise is then estimated through summation of the respective radial contributions that are calculated based on the local and overall operational conditions. Typically, the contribution of blade tip noise, attributable to 3D tip vortex formation, is negligible. An acoustically driven blade design conventionally foresees a reduced loading, i. e. reduced power production in the very tip region. Since published field test data are still limited, the relevant literature does not provide clear statements concerning the importance of additional flow-induced noise sources, i. e. flow separation noise and turbulent-inflow leading-edge interaction noise. The noise ranking of the latter two contributions appears individually dependent on the turbine type and site quality.

2. General approach

The project BELARWEA* aims at an extension of today's aeroacoustic evaluation and design capabilities in wind energy; current analyses are predominantly based on a 2D assessment, whereas full-3D evaluations are generally not considered due to non-affordable computational expenses. The prediction of 2D-profile TEN has been successfully documented in the BANC† framework [14, 15]. Moreover, the noise reduction efficiency of TE modifications (porous TE add-ons like serrations, brushes, etc.) has been previously verified at 2D blade sections [28]. However, these forerunner 2D studies still lack a systematic clarification to which extent the derived results can be transposed to full-scale rotational rotor geometries. The current experimental study intends to cover the first step from 2D to 3D static conditions, whereas in a future - planned - second phase of the project also the particular effects of the rotation are sought to be identified. The major objective lies in the provision of high-quality validation data for both 2D-based and 3D CAA prediction methods. A fully 3D numerical evaluation methodology would offer the mid-term perspective to add more degrees of freedom in today's design processes.

2.1. 2D numerical assessment

Figure 1 gives a general overview of the hybrid CFD/CAA prediction approach applied to support the design of a new profile contour RoH-W-18%c37. Profile design was conducted in an iterative process using the panel method XFOIL [3] with successive aeroacoustic evaluations. The current paper restricts to the description of the latter 2D acoustic evaluation procedure, whereas ongoing full 3D simulation work will be published in the future.

*The German acronym BELARWEA ("Blattspitzen für Effiziente und LärmArme Rotoren von WindEnergie-Anlagen") stands for "blade tips for efficient and low-noise wind turbine rotors".

†AIAA/CEAS Workshops on Benchmark Problems for Airframe Noise Computations

In a first analysis step, a steady RANS computation is performed by use of the DLR TAU-code [11, 27]. The CFD provides a time-averaged turbulent flow around the airfoil and the related turbulence statistics. In a second step, the DLR CAA-solver PIANO [2] is applied. Time-dependent linear propagation equations are solved on structured multi-block (SMB) meshes to compute the sound field. The resulting acoustic quantities, i. e. the spatially and time-resolved sound pressure, the acoustic particle velocity, or the sound intensity can be evaluated at user-selected microphone positions. These are usually located circularly around the trailing edge at a certain distance larger than the chord length l_c (here: $r_{\text{mic}} = 2.5\, l_c$).

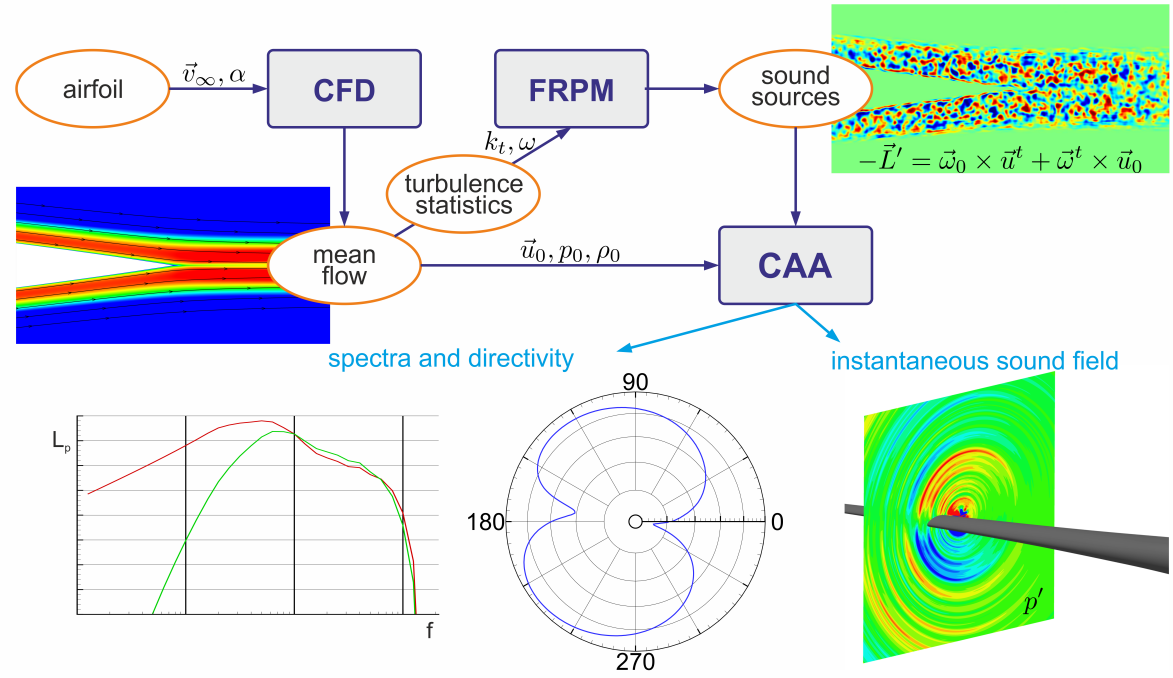

Fig. 1 Schematic of the hybrid RANS-based CAA prediction method.

On the right-hand side of the linear propagation equations, sound sources are explicitly imposed. A synthetic turbulence method provides fluctuating vorticity according to the turbulence statistics of the RANS solution. The Fast Random Particle-Mesh method (FRPM) [4, 5, 7, 8] realizes time-dependent fluctuations from time-averaged turbulence statistics. The standard method applied in this paper generates Gaussian correlated synthetic turbulence of local integral length scale and variance proportional to the turbulence kinetic energy distribution.

The steady time-averaged RANS flow provides the mean-flow over which the CAA simulation is carried out. Furthermore, the turbulence statistics provided by RANS is utilized to generate the unsteady vortex sound sources that drive the governing equations. In free field, this turbulence is coupled with the CAA solver, which is based on the 4$^{\text{th}}$ order accurate DRP scheme proposed by Tam & Webb [29]. The temporal discretization is realized by a low-dissipation, low-dispersion Runge-Kutta (LDDRK) algorithm by Hu [17]. Sound due to the interaction of vorticity with the trailing-edge is generated as part of the CAA simulation step. These vortex dynamics are dominated by the linear contributions to the source terms.

Farfield TEN data are scaled to represent 3D sound pressure level spectra at a span of s_{norm} = 1 m and a microphone distance of r_{norm} = 1 m. A 2D/3D scaling is applied as presented by Ewert et al. [6],

taking into account the local Ma number and setting the model constant in Eq. (1) as $\zeta = 1.4$. Based on a definition of the spanwise coherence length scale Brooks & Hodgson [1] report $\zeta = 1.4 \ldots 1.6$.

$$\Delta L_{p,i}^{\text{norm}} = \underbrace{10 \log_{10} \left(\frac{\zeta}{2\pi} \frac{s_{\text{norm}}}{r_{\text{mic}}} \text{Ma} \right)}_{\text{2D to 3D correction}} + \underbrace{20 \log_{10} \left(\frac{r_{\text{norm}}}{r_{\text{mic}}} \right)}_{\text{distance normalization}} \quad (1)$$

The prediction quality of this approach was previously documented along with code-to-code and experimental data comparisons within BANC category 1 (TEN) [14, 22, 23] and continuing benchmark activity with wind energy industry [9].

2.2. Test description

Tests were conducted in both the closed (3.25 m × 2.80 m) and ¾-open test sections of the Low-speed Wind-Tunnel Braunschweig DNW-NWB. Experiments in the closed test section served to measure the aerodynamic coefficients and to characterize the tip vortex flow fields. An overview of the model variants is provided in Figure 2. The BELARWEA reference blade tip is a 1:6 down-scaled derivative of the outer 20% radius portion of the NREL-5-MW-reference rotor [18] which is based on NACA 64-618 profile sections. Corresponding local chord lengths l_c are listed in 1 along with the positioning of the sections with static pressure measurement instrumentation. 4 Kulite-sensors (pinhole arrangement with a 0.4-mm diameter) were placed in close vicinity of the TE in sections 1–4 on the suction side of each model. The model span (span-wise coordinate: z with origin at model root) amounts to 2.1 m.

Table 1 Definition of the instrumented blade sections 1–5 (c_p: distributions of static pressure coefficients) with reference to the blade element numbers '#' of the NREL 5 MW rotor blade according to Jonkman [18]. R, r; rotor radius.

#	1:1		NWB (1:6)				comment
	R	% R	c_p	r, m	z, m	l_c, mm	
-	50.40	80.00	-	8.40	0.000	356.4	root profile
14	52.75	83.73	1	8.79	0.392	352.6	
15	56.17	89.15	2	9.36	0.961	344.3	
16	58.90	93.49	3	9.82	1.417	322.7	
-	59.98	95.20	4	10.00	1.596	300.9	
-	60.48	96.00	-	10.08	1.680	287.5	partition line to winglets
17	61.63	97.83	5	10.27	1.872	231.3	configurations without winglets

The tip planform in the outer 2.2% of the rotor radius has been arbitrarily defined based on usual tip geometries[‡]. To account for the static wind-tunnel conditions the original blade twist was removed

[‡]Thanks are due to the advisory board of the BELARWEA project, particularly to S. Erbslöh, Senvion GmbH. Note that the NREL 5-MW model rotor [18] is defined in terms of blade elements only and lacks a detailed tip planform geometry definition.

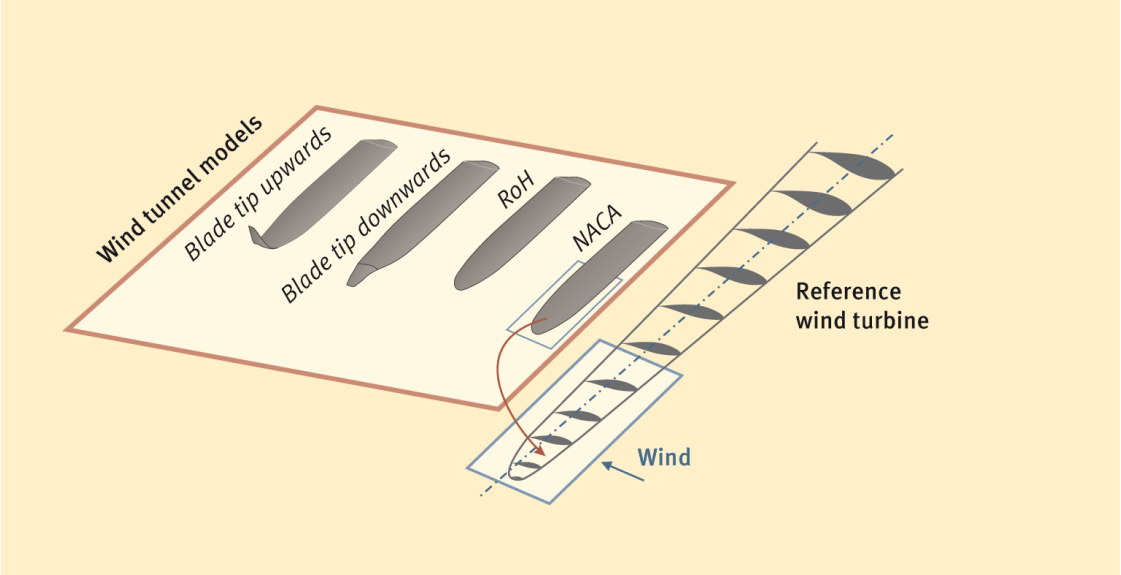

Fig. 2 DNW-NWB wing tip model variants.

and the chord distribution adjusted in radial (rotor) / spanwise (wind-tunnel) direction to consider the effect of varying local flow speed on local Reynolds numbers in the rotational case. Three additional blade tip variants are based on the new profile geometry RoH-W-18%c37; one with an identical planform and zero twist as the reference and the remaining two with exchangeable winglet geometries replacing the original tip. The two model variants without winglets were tested with brush retrofit devices based on a preselection made during the forerunner 2D AWB studies [28].

Tests in the closed test section served to measure the aerodynamic coefficients and to characterize the tip vortex flow fields. Acoustic measurements in the ¾-open test section comprised

- sound source identification with two phased microphone arrays, array 1 (~3 m diameter, 140 microphones) facing the suction side (SS) of the model and array 2 (~1 m diameter, 96 microphones) its pressure side (PS);
- TEN measurements in the approximate 2D-region of the model with a directional microphone system (elliptical mirror with 1.6 m diameter);
- comparative measurements with free field reference microphones;
- measurements of the hydrodynamic surface pressures close to the TE in different spanwise sections further characterized by static pressure distribution measurements, cf. Table 1.

Figure 3 gives an overview on the acoustic measurement setup. The obtained measurement database is applicable to (i) the validation of 2D-based TEN predictions and (ii) full 3D tip noise predictions. The validation concept for TEN predictions is shown in the bottom figure.

The model variants with RoH-W-18%c37 vs. NACA-64-618 profiles were tested for varying tripping conditions; the used denominations ‘NAT’ and ‘FUL’ accordingly refer to non-tripped turbulent boundary layers (TBL) with corresponding natural transition and tripped TBL, respectively. For configuration ‘FUL’ zigzag strips of 0.4 mm thickness were applied at 5% chord on the SS and 10% chord on the PS. Infrared thermography measurements confirmed the efficiency of the tripping devices. An additional configuration ‘NATFIX’ was introduced to ensure well-defined comparisons with the AWB measurements; in this configuration, boundary-layers were tripped at 42% chord on the SS and 52% chord on the PS to suppress the generation of a laminar separation bubble at the SS of the RoH-W-

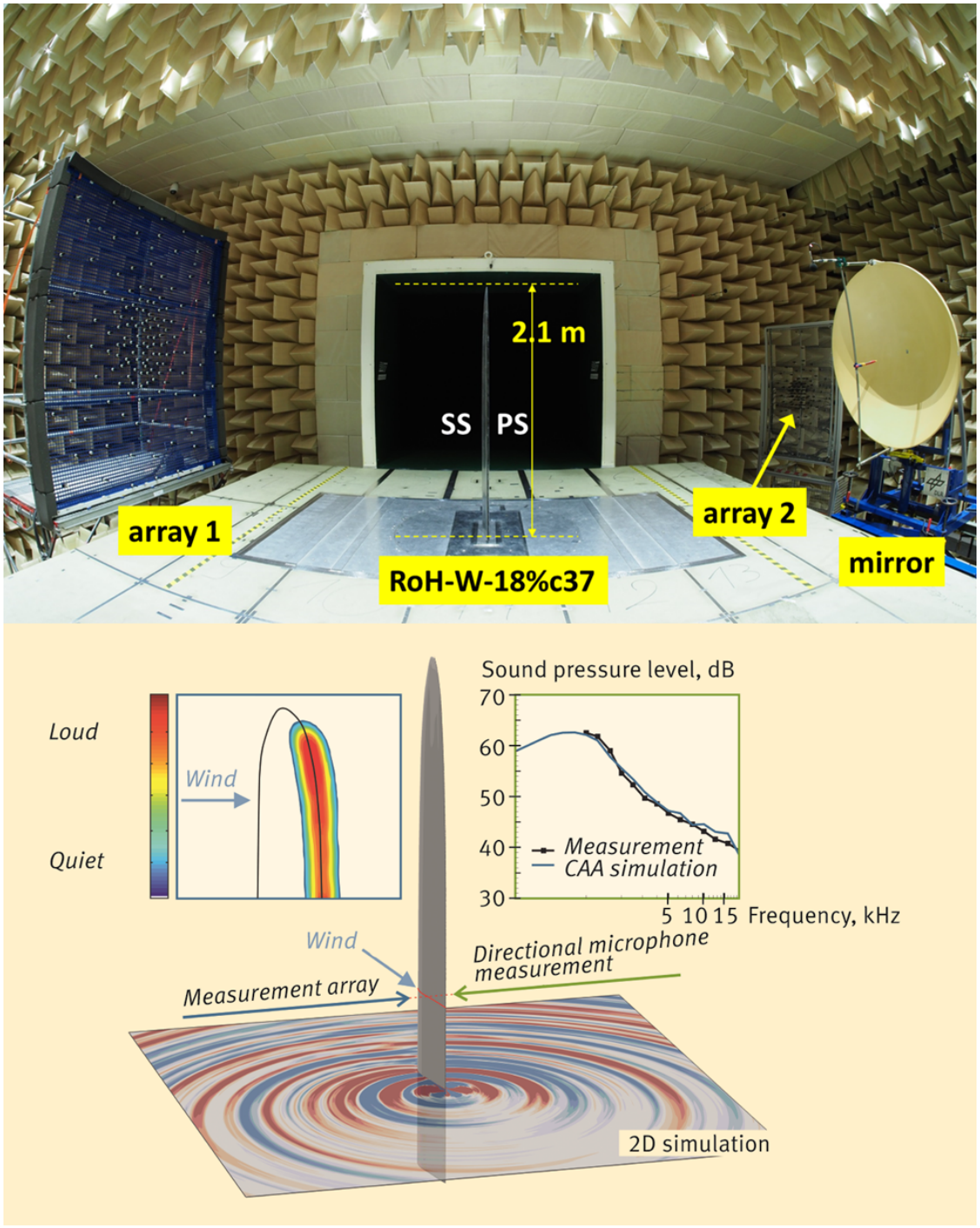

Fig. 3 DNW-NWB test setup and validation concept for 2D-based TEN prediction method.

18%c37 profile [28]. Note that the data post-processing is still ongoing; the following presentation of results will concentrate on the variants without winglets. The smaller array 2 was mainly dedicated to capture directivity effects induced by the winglets so that corresponding results will be retained for future communication on full 3D simulation and validation.

3. Results

3.1. 2D numerical results

The 2D numerical predictions obtained during the design process prior to the measurements are summarized in Figure 4; results refer to section 2 with l_c = 0.3443 m. Overall sound pressure levels OASPL are presented for stream velocities of u_∞ = 60 m/s and u_∞ = 80 m/s along with profile lift coefficients c_l, lift-over-drag ratios c_l/c_d and angles-of-attack α. Accordingly, an OASPL reduction of about 2–2.5 dB was expected for the design lift coefficient c_l = 1.15.

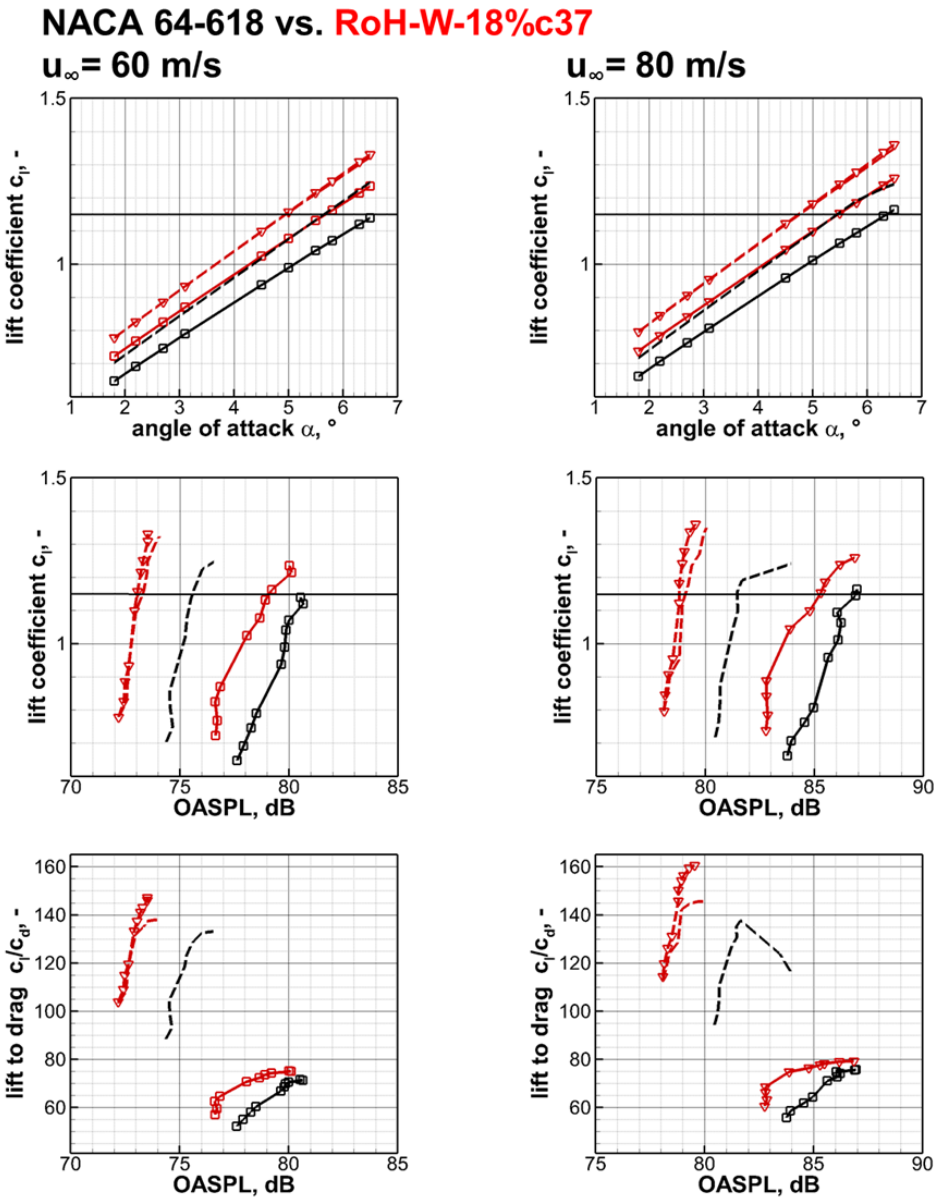

Fig. 4 2D CFD/CAA predictions for the NACA 64-618 (black color) vs. RoH-W-18%c37 (red color) profile contours. Symbols denote tripped configurations; i. e. FUL (solid lines) or NAT-FIX (dashed lines), dashed lines without symbols indicate natural transition NAT.

3.2. General overview on the DNW-NWB test data

The current setup in the DNW-NWB served with extended ranges of test parameters when compared to the preparatory studies at 2D blade sections in AWB with comparable chord (AWB: l_c = 0.3 m); i. e. tests could be performed at larger angles-of-attack (larger model aspect ratio of 6.7 compared to 2.7 in the AWB) and test velocities of up to 80 m/s (compared to 60 m/s in AWB). Moreover, due to the cantilever setup the background noise from the corner junctions (side-plates in AWB, test section floor in NWB) was reduced so that the usable frequency range could be extended below 1 kHz, the well-documented low-frequency limit in most of the published TEN experimental data. TEN peak frequencies are consequentially expressed in both Kulite (source) and farfield TEN data. TEN data in the spectral peak region appear still contaminated by the junction, however, to a lower extent when compared to AWB test conditions.

A first tentative cross-comparison of results from 2D blade section measurements in AWB vs. the blade tip model measurements in DNW-NWB is provided in Figure 5 along with 2D CFD/CAA predictions for configurations RoH-W-18%c37 FUL and NATFIX. AWB prediction and measurement results are scaled from u_∞ = 50 m/s to u_∞ = 80 m/s. One-third octave band sound pressure levels $SPL_{1/3}$ in

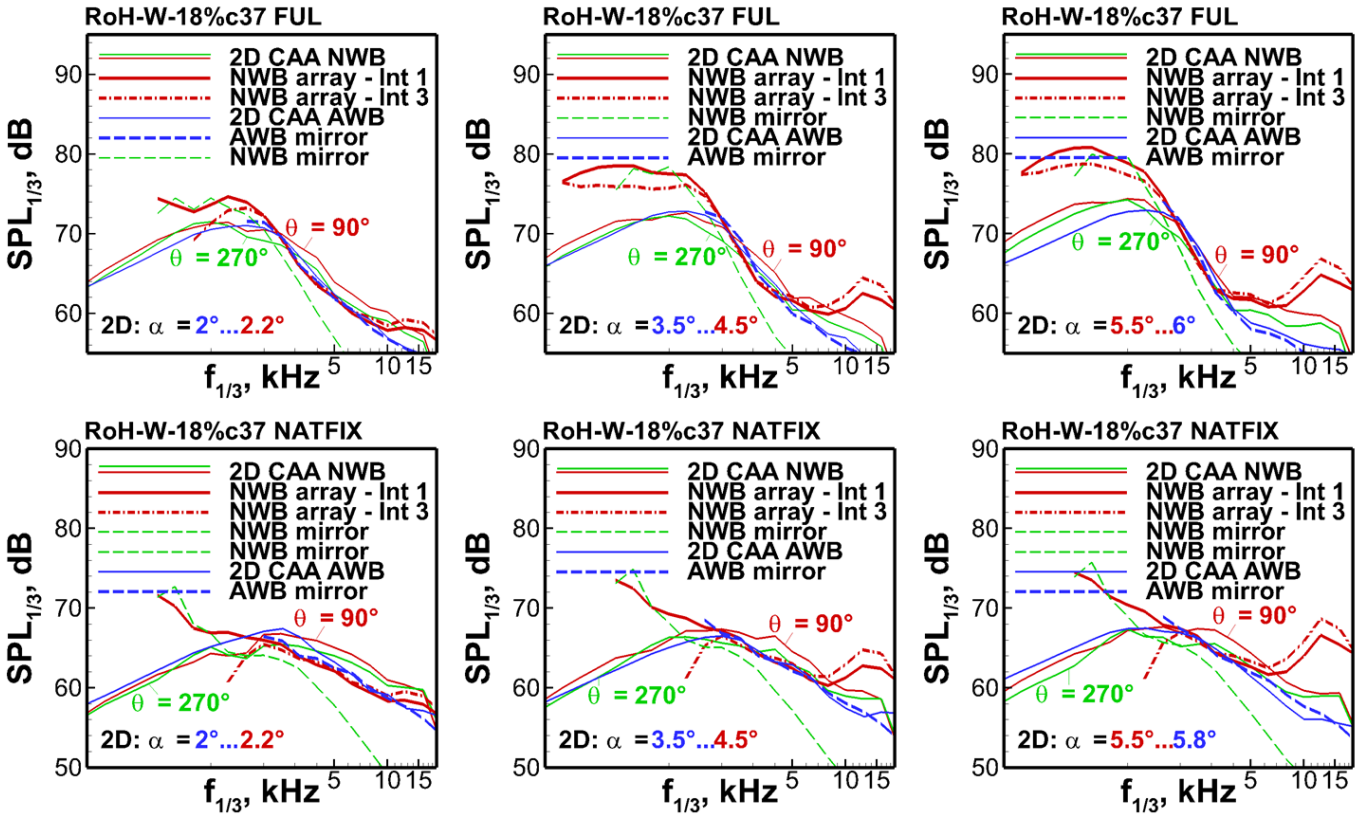

Fig. 5 Comparison of 2D CFD/CAA predictions with measurements at the RoH-W-18%c37 configuration, u_∞ = 80 m/s. The directivity angle θ refers to the wind-tunnel center line and to the TE position at α = 0°; θ = 90° (red color) corresponds to the position of the center microphone of array 1 facing the SS, θ = 270° (green color) to the convection-corrected focus position of the directional microphone system facing the PS (same definition, i. e. θ = 270°, holds for the AWB setup marked by blue color).

this representation format are arbitrarily normalized to a 1-m span and a 1-m distance. The shown microphone array data sets are based on a first assessment by means of standard beamforming, as provided by DNW-NWB directly after the test. Given the selected integration areas, it is not expected that spectral maxima will have to perfectly collapse with 2D simulations or AWB measurements, respectively. The integration areas are displayed in the Appendix, cf. Figure 13; Int 1 covers the whole model (2.1 m), whereas Int 3 (span: 1.4 m) excludes the floor region to initially suppress noise by the floor junction. Again, NWB conditions are selected based on local conditions at section 2, where also the elliptical mirror far focus was set. Aerodynamic angles-of-attack α were not exactly identical for both test environments (blue: AWB; red: NWB), but close enough to derive the following interim conclusions:

- Directional microphone and array measurements in DNW-NWB lead to consistent results; low-frequency peak levels which are dominated by floor-junction noise at least for the quieter model configurations (i. e. NATFIX and NAT) are of same order when comparing red solid lines (NWB array Int 1) with green dashed lines (NWB mirror). Due to the TEN directivity it is expected that for non-zero angles-of-attack levels beyond the TEN peak should be lower for the measurement systems facing the PS of the model, cf. the 2D simulation results for orders of magnitude. However, spectral decay slopes in the mirror spectra appear over-corrected by the herein applied theoretical gain and resolution assumptions according to Schlinker [12, 26]. Note that an in-situ calibration of the directional microphone system (as available for the smaller 1.4-m-diameter AWB directional microphone system) could not be afforded during the BELARWEA campaign. The latter is foreseen in the future to guarantee comparable data reliability as in the AWB.
- 2D simulation and AWB 2D blade section measurement results show almost perfect agreement, whereas discrepancies in spectral shape appear for the wing tip model spectra. Spectral decay slopes beyond the TEN peak are almost identical for the wing tip array data. This is an unexpected result if assuming the overall TEN of the wing tip model to be the result of an independent summation of slice-wise 2D TEN contributions.
- Deviations between 2D and wing tip model results are observable in the peak region and at frequencies around 10–15 kHz where tip noise contributions appear in the microphone array source maps, cf. Figure 6. The relative importance of the latter is dependent on the configuration. Exact reconstruction of absolute TEN peak levels and a clear identification of 3D effects on TEN spectra will require the application of more advanced array data post-processing methods to i) reliably correct for excess noise contributions and to ii) enabling a more detailed separation of overall noise into smaller section-wise contributions.

Some additional example results are shown below in Figures 6– 8 to illustrate the extent of the acoustic database. The noise reduction effect of brush TE devices was demonstrated, see Figure 6. However, due to the installation conditions at the wing tip model the achieved overall noise reduction (of up to 6 dB) was slightly reduced when compared to the results obtained in the AWB [28] under idealized 2D conditions.

For the same selected model configurations with and without brush the effects of test angle-of-attack (Figure 7) and velocity (Figure 8) are shown in terms of unsteady surface pressure narrowband spectra (figures left) and one-third-octave band spectra of farfield TEN (figures right), as measured with the directional microphone system. Note that the brush TE does not significantly affect the incoming hydrodynamic pressures in the source region.

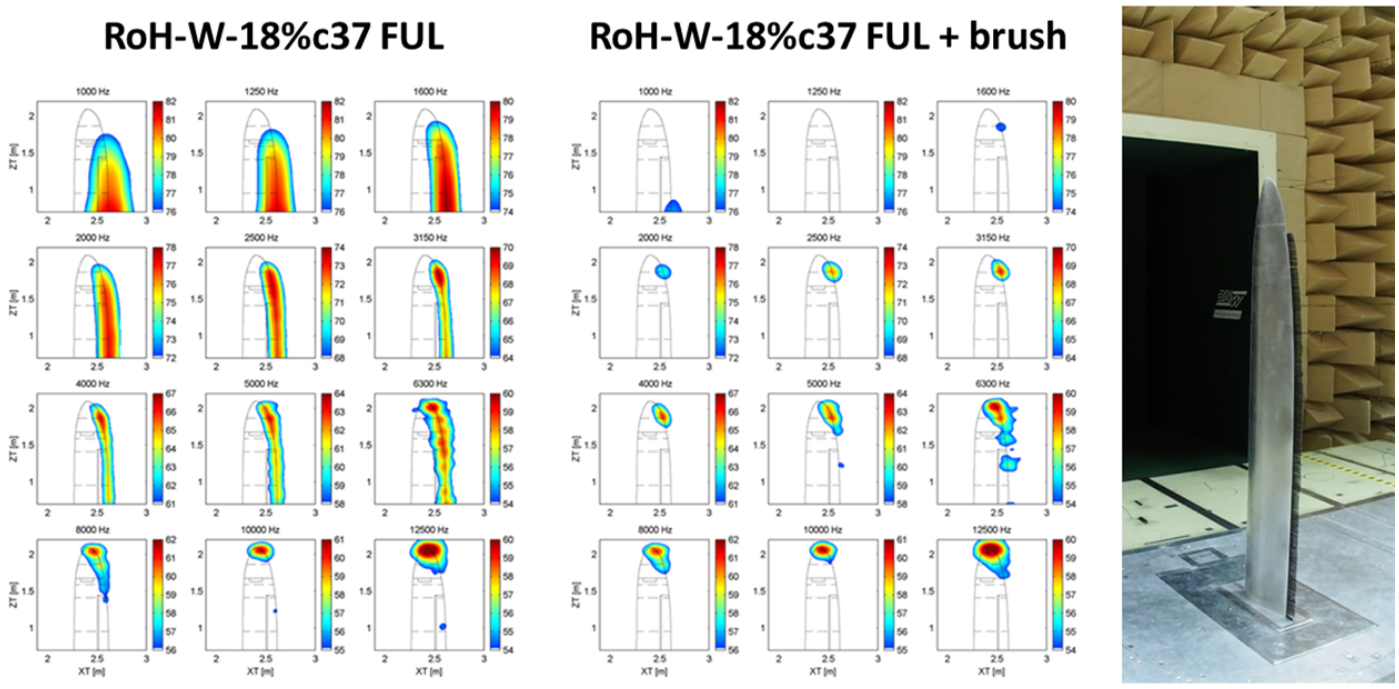

Fig. 6 Source maps from standard beamforming (microphone array 1, pointing to the SS, in 1/3-octave bands) for α = 3.1° and u_∞ = 80 m/s. Brush extends to z_T = 1.835 m.

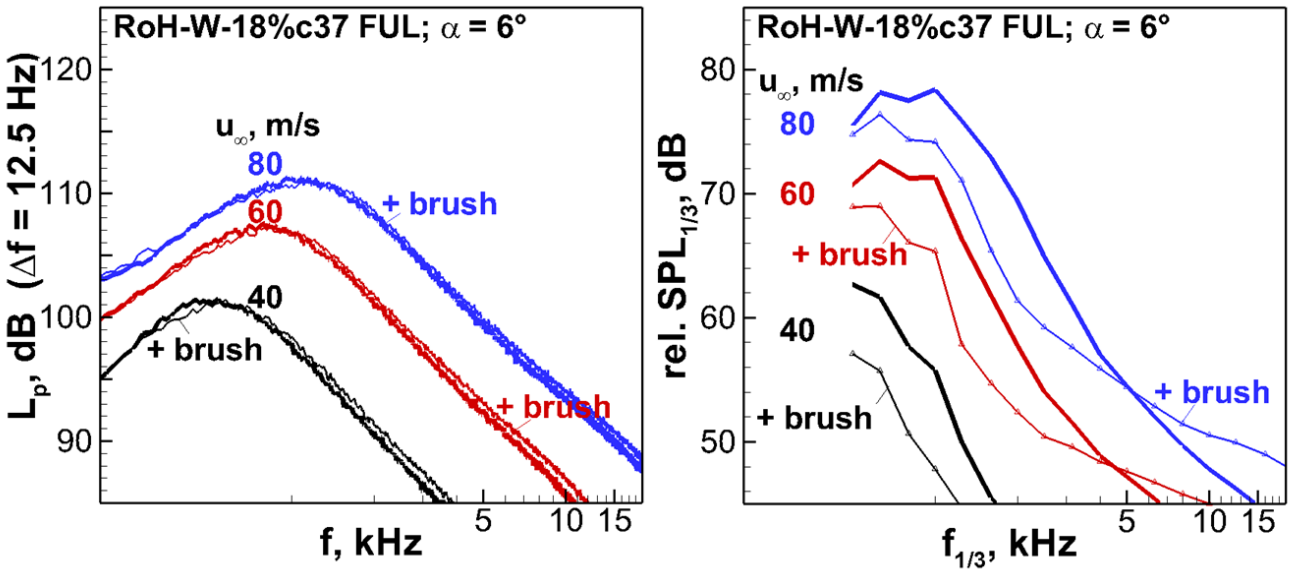

Fig. 7 Effect of flow speed on (left) surface pressure narrowband spectra (Kulite No. 2 at the height of the elliptic mirror focus, Δf = 12.5 Hz, re. 20 μPa) and TEN farfield noise (elliptic mirror data when focusing at the convection-corrected TE location at z = 0.9611 m), α = 6°.

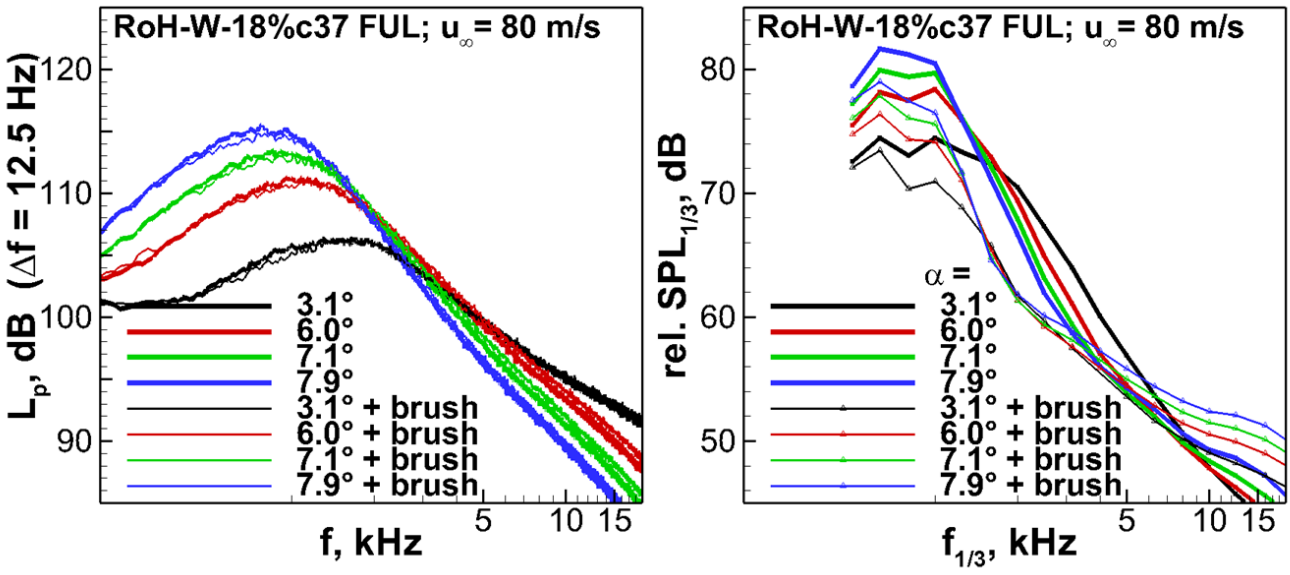

Fig. 8 Effect of test angle-of-attack on (left) surface pressure narrowband spectra (Kulite No. 2, Δf = 12.5 Hz, re. 20 μPa) and TEN farfield noise (elliptic mirror data when focusing at the convection-corrected TE location at z = 0.9611 m), u_∞ = 80 m/s.

3.3. Aeroacoustic evaluation of the RoH-W-18%c37 profile design

In the following, a selection of key figures are provided, documenting the noise reduction effect of the RoH-W-18%c37 profile contour, when compared to the NACA 64-618 reference. For better readability, the same color coding for the two model variants as in Figure 4 is kept in the remainder of this report; red color refers to the RoH-W-18%c37 contour and black color to the NACA 64-618 reference.
The aerodynamic conditions selected for the subsequent aeroacoustic evaluation are given in Figure 9 and Tables 2 to 3. Figures 10 and 11 summarize measured surface pressure spectra close to the TE for the TBL configurations NAT and FUL at four different spanwise positions. Static pressure distributions at the respective sections can be found in the Appendix, cf. Figures 14 and 15, indicating moderate flow separation for the configuration NACA 64-618 FUL already at α = 8.1°.

Table 2 Comparison conditions with approximately equal lift (TBL configuration NAT); geometric vs. corresponding aerodynamical angles of attack (α_g/α) for c_L-values in Figure 9.

NAT	c_L = 0.75...0.76	c_L = 1.02...1.03	c_L = 1.12	c_L = 1.14...1.15
NACA 64-618	4.6°/3.8°	8.0°/7.0°	9.5°/8.4°	10.0°/8.8°
RoH-W-18%c37	3.8°/3.0°	7.0°/5.9°	8.2°/7.0°	8.5°/7.3°

Corresponding farfield sound measurement results are represented in Figure 12 for configurations NAT (top) and FUL (bottom). The figures also contain the predicted TEN spectra for local conditions at section 2. Measured and simulated c_p distributions are shown on the top of each set of

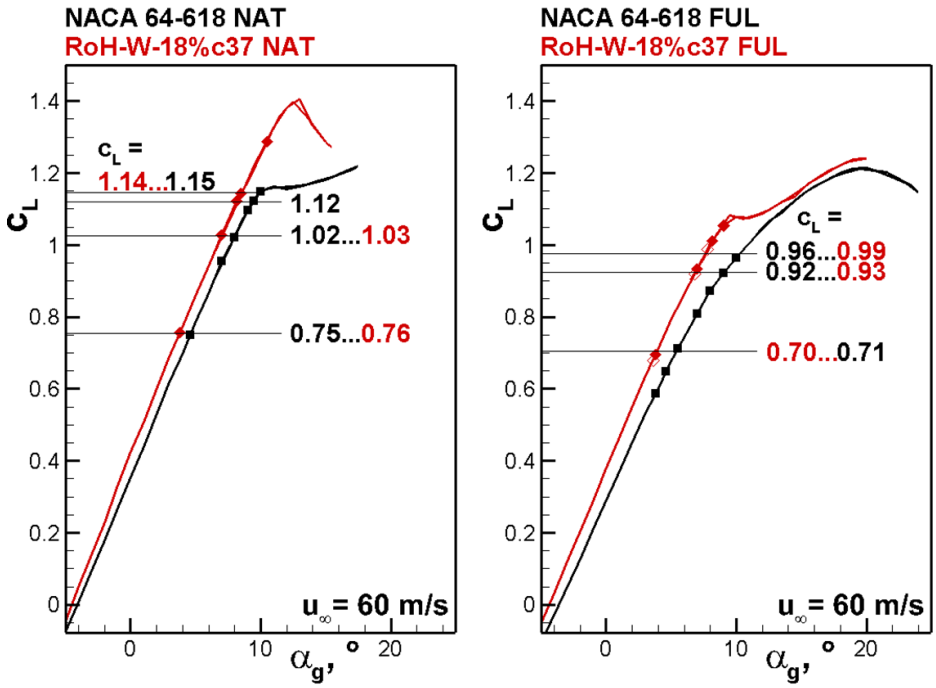

Fig. 9 Total lift coefficients c_L vs. geometric angles of attack α_g from force balance measurements (3/4-open test section, as measured). Filled symbols denote available acoustic measurements for these conditions at u_∞ = 40; 60; 70; 80 m/s, open symbols mark additional data points for u_∞ = 60 m/s only .

Table 3 Same as Table 2 but TBL configuration FUL.

FUL	c_L = 0.70...0.71	c_L = 0.92...0.93	c_L = 0.96...0.99 (1.01)
NACA 64-618	5.5°/4.8°	9.0°/8.1°	10.0°/9.0°
RoH-W-18%c37	3.8°/3.1°	7.0°/6.0°	7.8°/6.8° (8.2°/7.1°)

figures. As expected from the design specifics and previous AWB measurements, configuration RoH-W-18%c37 NAT features a laminar separation bubble (with turbulent reattachment) at the SS that can be suppressed by tripping slightly upstream (configuration NATFIX). Equivalent available measurements at both the NACA 64-618 and the RoH-W-18%c37 variants in configuration NATFIX have shown consistently modulated spectra for both airfoils so that the received level differences are not significantly affected by selection of the respective tripping configuration. To reduce the number of graphs in this overview the presentation of results is limited to configuration NAT.

Overall, the observed trends in both Kulite measurement data and 2D CAA predictions are well-represented in the farfield TEN measurement data, i. e. significant reductions of the TEN peak levels are documented. The reduction in peak level increases with angle-of-attack. It is, however, accompanied by a corresponding noise increase at mid-to-high frequencies which would indeed lead to slightly reduced OASPL reductions, when A-weighting is applied. In particular for configuration NAT the measured frequency of the crossing location of the two spectra is perfectly captured by the

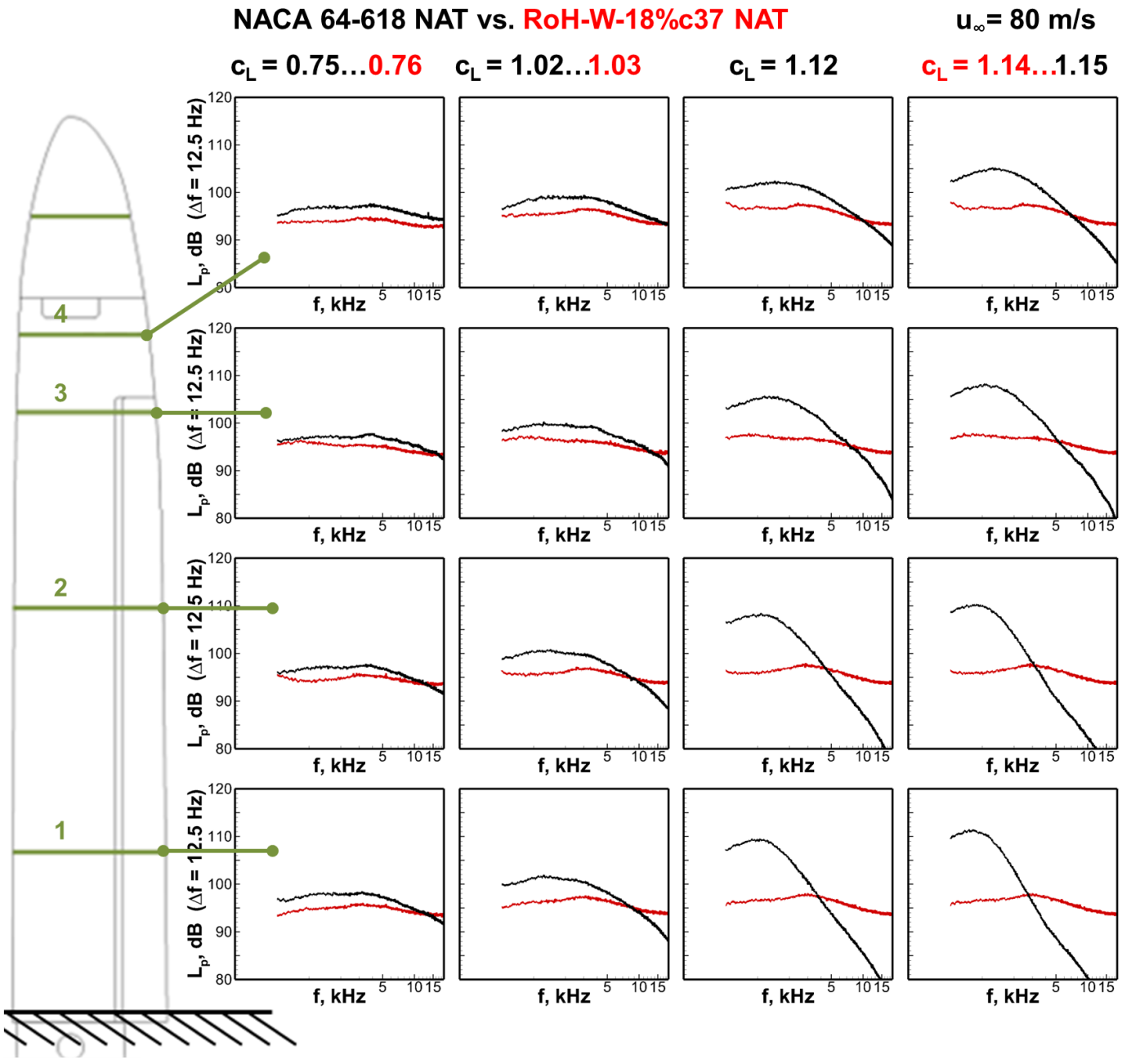

Fig. 10 Measured surface pressure narrowband spectra (re. 20 μPa) for configuration NAT.

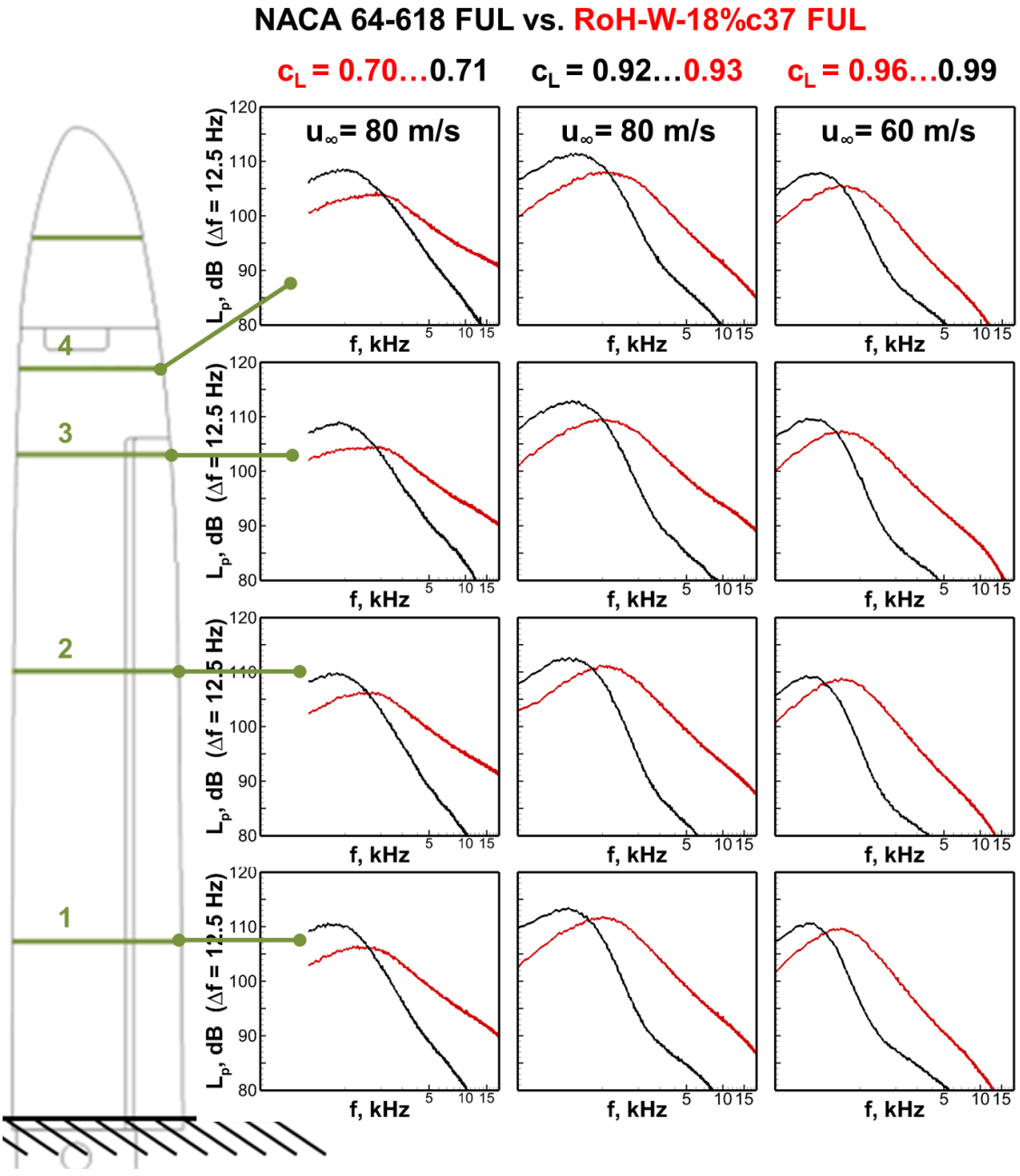

Fig. 11 Measured surface pressure narrowband spectra (re. 20 μPa) for configuration FUL.

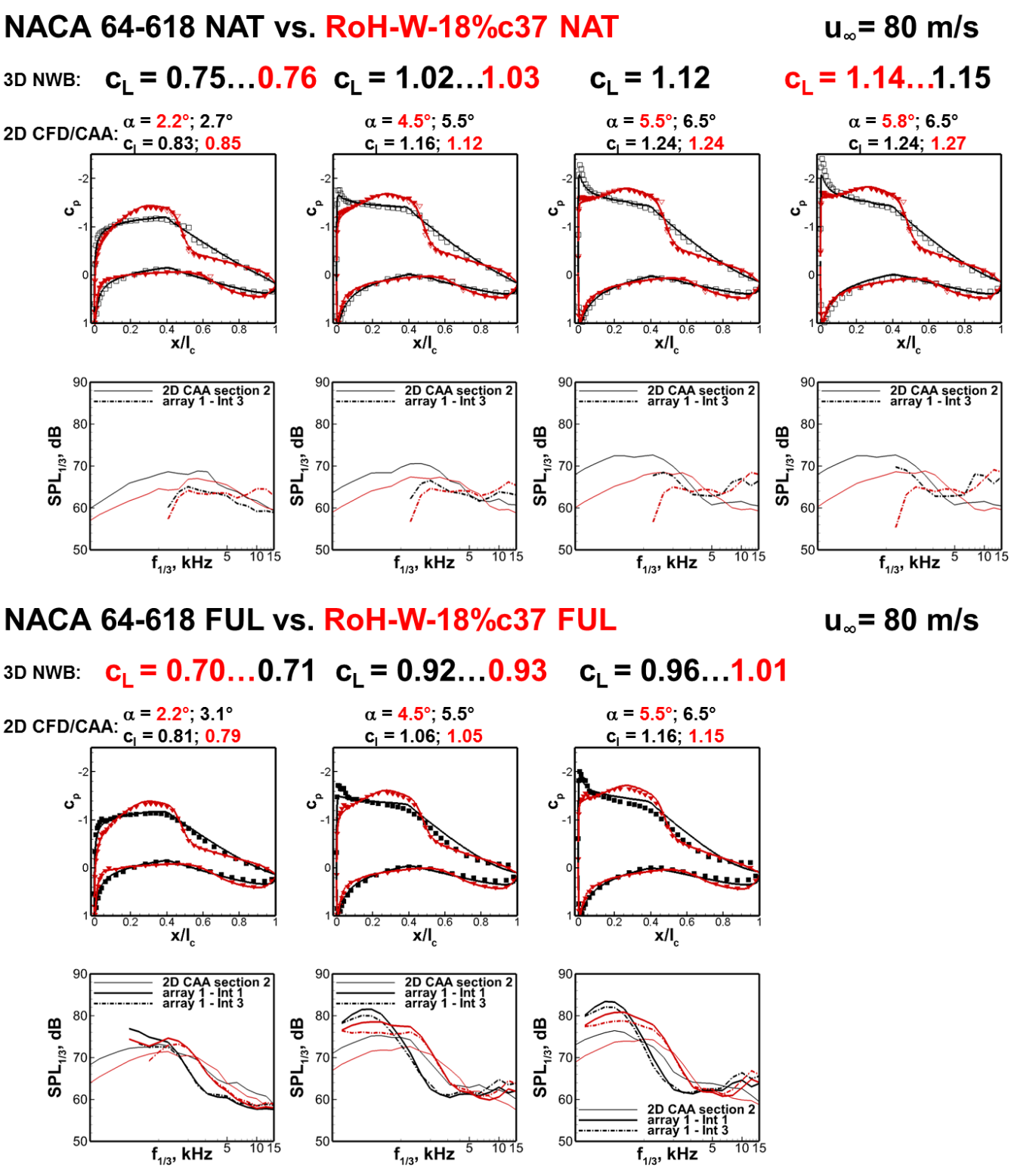

Fig. 12 1/3-octave band farfield TEN spectra (bottom line of figures), as measured with the microphone array 1, compared to 2D prediction results for conditions in section 2 and corresponding measured (symbols) and simulated (solid lines) c_p distributions (top line of figures). Filled symbols refer to tripped configurations FUL and NATFIX, open symbols to configuration NAT.

2D CAA predictions. This is lesser the case for configuration FUL because the flow separation at the NACA 64-618 is not reproduced in the 2D CFD results.
A-weighted representations of levels are omitted here because these are considered meaningful only for full scale conditions, being based on a previously specified (i. e. realistic) turbine application. The interested reader might refer to reference [13], where non-weighted and A-weighted results are shown for the original BELARWEA design conditions which where different from either AWB or NWB conditions. Design conditions were focusing at a projected experimental turbine and, therefore, represent a compromise between typical full scale and wind-tunnel conditions.

4. Conclusion and outlook

The present paper wraps-up first results from an extensive set of aeroacoustic experiments conducted in the framework of the German project BELARWEA. Small-scaled wind turbine blade tip models were systematically tested over a broad range of test parameters in the acoustic wind tunnel DNW-NWB, hence, supplementing previous tests at 2D blade sections in the smaller acoustic test facility AWB. Both experimental and numerical studies are reported aiming at the successful demonstration and validation of existent DLR noise prediction methodologies. A 2D-based, largely non-empirical prediction method was applied to support the design of a new airfoil contour RoH-W-18%c37. When compared to a NACA 64-618 reference contour, a 2–4 dB reduction of maximum sound pressure levels, corresponding to an OASPL reduction of 2–2.5 dB was predicted for the design lift coefficient c_l = 1.15. Measured noise reductions at the blade tip models at equivalent conditions perfectly confirm this design target. Application of brushes has been documented to achieve an additional noise reduction effect that can reach up to ~6 dB. However, the used validation/verification data base will have to be further analysed and improved prior to derive further conclusions on detailed 3D effects on noise generation. Apart from excess noise contributions from the model/floor junction, maximum noise levels are induced by trailing-edge noise (TEN) at low- to mid frequencies while noise contributions from the outer tip regions are located in the higher frequency range. The latter can reach significant levels comparable to the low-frequency peak, if a large laminar extent of the boundary layer can be realized.
Future steps will include an improved (slice-wise) post-processing of the available microphone array data for a better comparability of derived absolute sound pressure levels as measured on 2D wing sections in AWB and portions of the blade tip models in DNW-NWB. Moreover, more advanced deconvolution algorithms will be systematically applied in hopes to better suppress present excess noise contributions originating from the floor/model junctions. An on-site recalibration of the 1.6-m-diameter acoustic mirror system in DNW-NWB is considered worthwhile to quantify and correct for potential shear-layer-induced signal losses that might explain the unexpected steep slopes of the TEN spectra when compared to corresponding microphone array results and AWB acoustic mirror data. The full measurement data base covering free stream velocities of 40 m/s up to 80 m/s will be further analyzed with regard to commonly known TEN scaling laws. Based on the correspondingly normalized data sets, the applied post-processing and resulting data validity ranges can be further examined.
Ongoing work includes the full 3D CFD/CAA evaluation of the winglet configurations by means of a new hybrid DLR method, combining the RANS-based stochastic turbulence model FRPM with an efficient propagation solver by means of a fast-multipole boundary element method (DLR code FMCAS) [24, 25]. The collected database will serve for validation of the new methodology.

Appendix

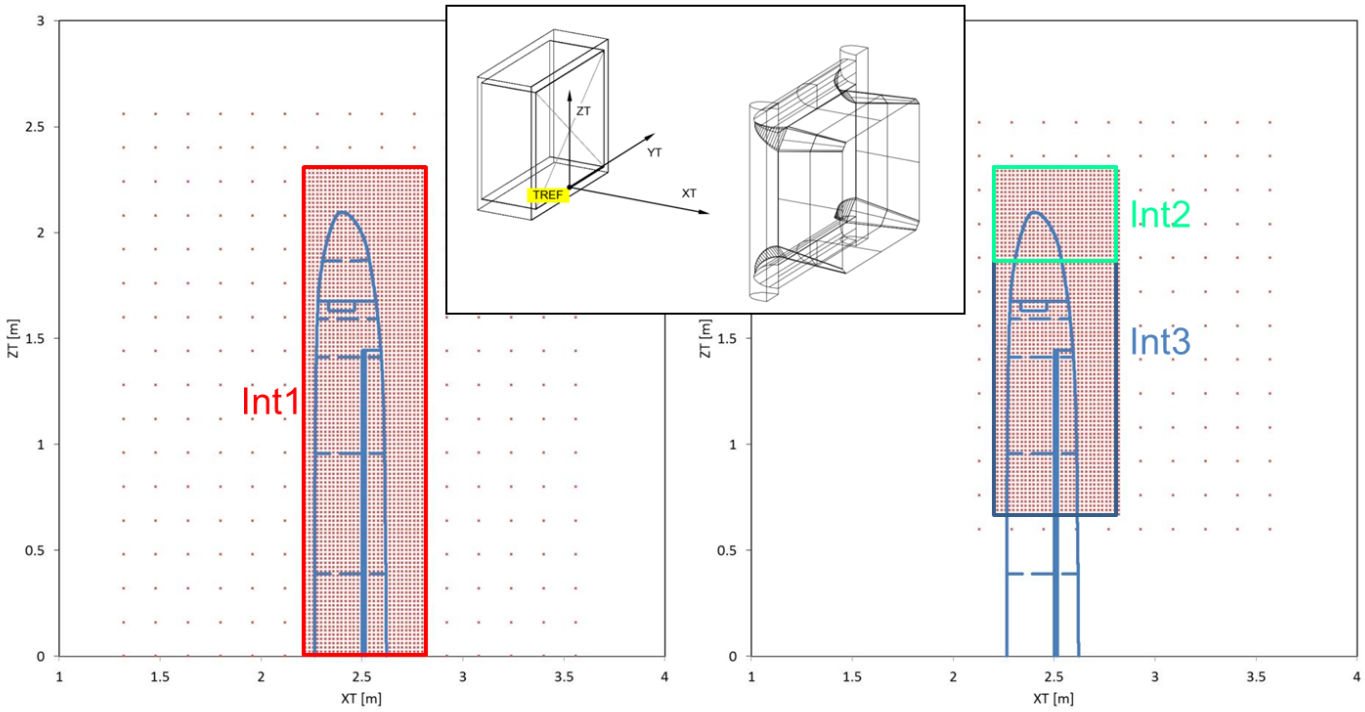

Fig. 13 Wind-tunnel coordinate system and integration areas used for the array post-processing.

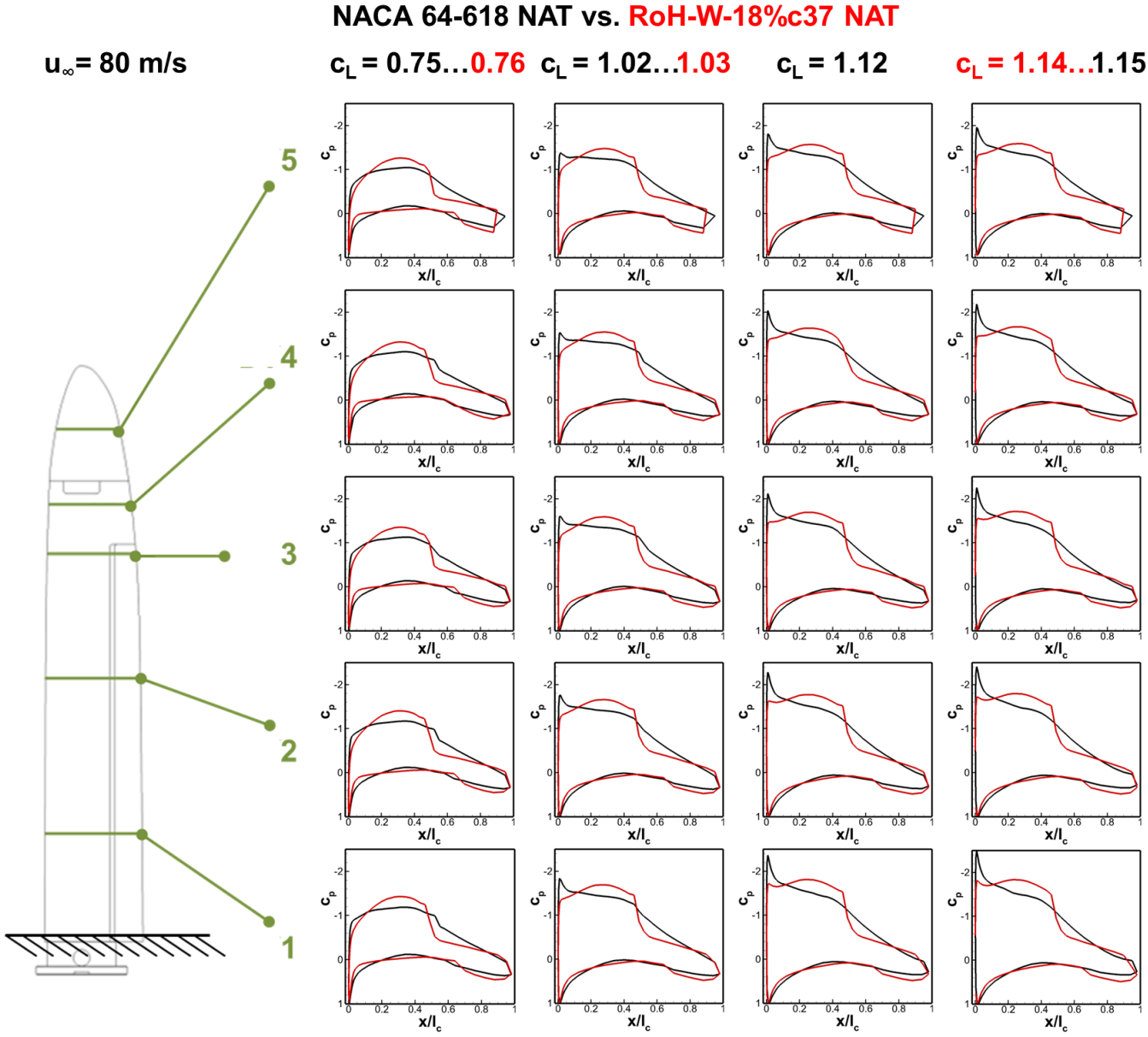

Fig. 14 Measured c_p distributions corresponding to Kulite measurement results in Figure 10.

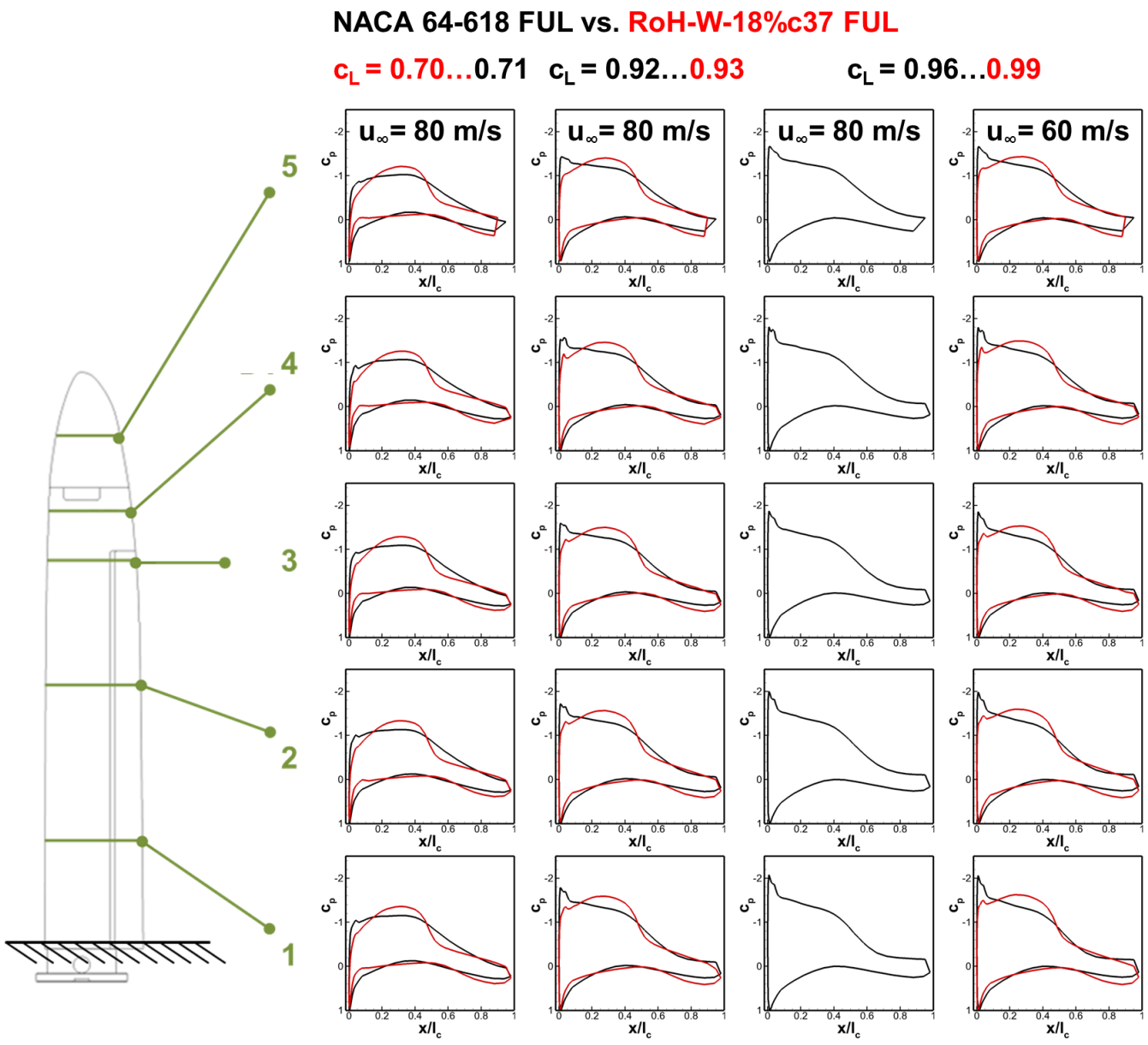

Fig. 15 Measured c_p distributions corresponding to Kulite measurement results in Figure 11.

Acknowledgments

This work has been conducted within the project BELARWEA (ref. 0325726) funded by the German Federal Ministry for Economic Affairs and Energy (BMWi). The authors are grateful to the BELARWEA consortium.

References

[1] Brooks, T. F. and Hodgson, T. H. (1981). Trailing Edge Noise Prediction from Measured Surface Pressures. *Journal of Sound and Vibration*, 78(1):69–117.

[2] Delfs, J. W., Bauer, M., Ewert, R., Grogger, H. A., Lummer, M., and Lauke, T. G. W. (2008). Numerical Simulation of Aerodynamic Noise with DLR's Aeroacoustic Code PIANO.

[3] Drela, M. (1989). An Analysis and Design System for Low Reynolds Number Airfoils. Conf. procs., Conference on Low Reynolds Number Airfoil Aerodynamics, University of Notre Dame, France.

[4] Ewert, R. (2007). RPM—the Fast Random Particle-Mesh Method to Realize Unsteady Turbulent Sound Sources and Velocity Fields for CAA Applications. AIAA Paper AIAA 2007-3506.

[5] Ewert, R. (2008). Broadband Slat Noise Prediction based on CAA and Stochastic Sound Sources from a Fast Random Particle-Mesh (RPM) Method. *Computers & Fluids*, 37:369–387.

[6] Ewert, R., Appel, C., Dierke, J., and Herr, M. (2009). RANS/CAA Based Prediction of NACA0012 Broadband Trailing Edge Noise and Experimental Validation. AIAA Paper AIAA 2009-3369.

[7] Ewert, R., Dierke, J., Siebert, J., Neifeld, A., Appel, C., Siefert, M., and Kornow, O. (2011). CAA Broadband Noise Prediction for Aeroacoustic Design. *Journal of Sound and Vibration*, 330(17):4139–4160.

[8] Ewert, R. and Edmunds, R. (2005). CAA Slat Noise Studies Applying Stochastic Sound Sources Based on Solenoidal Digital Filters. AIAA Paper AIAA 2005-2862.

[9] Ferret Gasch, O., Oerlemans, S., Faßmann, B. W., Herr, M., Bertagnolio, F., Fischer, A., Arnold, B., and Lutz, T. (2019). Trailing Edge Noise Prediction of Wind Turbine Airfoils: A Benchmark Exercise. AIAA Paper AIAA 2019-XXXX, number to be assigned.

[10] Ffowcs Williams, J. E. and Hall, L. H. (1970). Aerodynamic Sound Generation by Turbulent Flow in the Vicinity of a Scattering Half Plane. *Journal of Fluid Mechanics*, 40(4):657–670.

[11] Gerhold, T., Galle, M., Friedrich, O., and Evans, J. (1997). Calculation of Complex Three-Dimensional Configurations Employing the DLR-τ-Code. AIAA Paper AIAA 1997-0167.

[12] Herr, M. (2013). *Trailing-Edge Noise—Reduction Concepts and Scaling Laws*. Dissertation, Technische Universität Braunschweig, published as DLR Research Report 2013-32, ISSN 1434-8454, ISRN DLR-FB-2013-32.

[13] Herr, M., Ewert, R., Faßmann, B., Rautmann, C., Martens, S., Rohardt, C.-H., and Suryadi, A. (2018). Noise Reduction Technologies for Wind Turbines. *Notes on Numerical Fluid Mechanics and Multidisciplinary Design (NNFM)*, 136, Hrsg: A. Dillmann, G. Heller, E. Krämer, C. Wagner, S. Bansmer, R. Radespiel, R. Semaan, New Results in Numerical and Experimental Fluid Mechanics XI, Contributions to the 20th STAB/DGLR Symposium Braunschweig, Germany, 2016, Springer International Publishing AG:611–621.

[14] Herr, M., Ewert, R., Rautmann, C., Kamruzzaman, M., Bekiropoulos, D., Iob, A., Arina, R., Batten, P., Chakravarthy, S., and Bertagnolio, F. (2015). Broadband Trailing-Edge Noise Predictions—Overview of BANC-III Results. AIAA Paper AIAA 2015-2847.

[15] Herr, M. and Kamruzzaman, M. (2013). Benchmarking of Trailing-Edge Noise Computations—Outcome of the BANC-II Workshop. AIAA Paper AIAA 2013-2123.

[16] Howe, M. S. (1978). A Review of the Theory of Trailing Edge Noise. *Journal of Sound and Vibration*, 61(3):437–465.

[17] Hu, F. Q., Hussaini, M. Y., and Manthey, J. L. (1996). Low-Dissipation and Low-Dispersion Runge–Kutta Schemes for Computational Acoustics. *Journal of Computational Physics*, 124(1):177–191.

[18] Jonkman, J., Butterfield, S., Musial, W., and Scott, G. (2009). Definition of a 5-MW Reference Wind Turbine for Offshore System Development. NREL Technical Report NREL/TP-500-38060.

[19] Oerlemans, S. (2016). Reduction of Wind Turbine Noise using Blade Trailing Edge Devices. AIAA Paper 2016-3018.

[20] Oerlemans, S., Fisher, M., Maeder, T., and Kögler, K. (2009). Reduction of Wind Turbine Noise using Optimized Airfoils and Trailing-Edge Serrations. *AIAA Journal*, 47(6):1470–1481.

[21] Oerlemans, S., Sijtsma, P., and López, B. M. (2007). Location and Quantification of Noise on a Wind Turbine. *Journal of Sound and Vibration*, 299:869–883.

[22] Rautmann, C. (2017). *Numerical Simulation Concept for Low-Noise Wind Turbine Rotors*. Dissertation, Technische Universität Braunschweig, published as DLR Research Report 2017-35, ISSN 1434-8454, ISRN DLR-FB-2017-35.

[23] Rautmann, C., Dierke, J., Ewert, R., Hu, N., and Delfs, J. (2014). Generic Airfoil Trailing-Edge Noise Prediction using Stochastic Sound Sources from Synthetic Turbulence. AIAA Paper AIAA 2014-3298.

[24] Reiche, N., Ewert, R., and Delfs, J. (2016). Realization of Arbitrary Vorticity Spectra using Generic Stochastic Turbulence. AIAA Paper AIAA 2016-2964.

[25] Reiche, N., Lummer, M., Ewert, R., Delfs, J. W., and Alavi Moghadam, S. M. (2015). Towards High-Lift Noise from Fast Multipole BEM with Anisotropic Synthetic Turbulence Structures. AIAA Paper AIAA 2015-2672.

[26] Schlinker, R. H. (Oct. 1977). Airfoil Trailing Edge Noise Measurements with a Directional Microphone. AIAA Paper 77-1269.

[27] Schwamborn, D., Gerhold, T., and Heinrich, R. (2006). The DLR TAU-Code: Recent Applications in Research and Industry. In *ECCOMAS European Conference on Computational Fluid Dynamics 2006*.

[28] Suryadi, A., Martens, S., and Herr, M. (2017). Trailing-Edge Noise Reduction Technologies for Applications in Wind Energy. AIAA Paper AIAA 2017-3534.

[29] Tam, C. K. W. and Webb, J. C. (1993). Dispersion-Relation-Preserving Finite Difference Schemes for Computational Acoustics. *Journal of Computational Physics*, 107(2):262–281.